

The gas streamer G1-2-3 in the Galactic Center

S. Gillessen¹, F. Eisenhauer^{1,3}, J. Cuadra^{4,9}, R. Genzel^{1,2}, D. Calderon⁵, S. Joharle¹, T. Piran⁷, D.C. Ribeiro¹, C.M.P. Russell⁸, M. Sadun Bordoni¹, A. Burkert^{6,1}, G. Bourdarot¹, A. Drescher¹, F. Mang¹, T. Ott¹, G. Agapito¹⁰, A. Agudo Berbel¹, A. Baruffolo¹², M. Bonaglia¹⁰, M. Black¹³, R. Briguglio¹⁰, Y. Cao¹, L. Carbonaro¹⁰, G. Cresci¹⁰, Y. Dallilar¹⁶, R. Davies¹, M. Deyseroth¹, I. Di Antonio¹¹, A. Di Cianno¹¹, G. Di Rico¹¹, D. Doelman¹⁵, M. Dolci¹¹, S. Esposito¹⁰, D. Fantinel¹², D. Ferruzzi¹⁰, H. Feuchtgruber¹, N. M. Förster Schreiber¹, A. M. Glauser¹⁴, P. Grani¹⁰, M. Hartl¹, D. Henry¹³, H. Huber¹, C. Keller¹⁵, M. Kenworthy¹⁵, K. Kravchenko¹, J. Lightfoot¹³, D. Lunney¹³, D. Lutz¹, M. Macintosh¹³, F. Mannucci¹⁰, D. Pearson¹³, A. Puglisi¹⁰, S. Rabien¹, C. Rau¹, A. Riccardi¹⁰, B. Salasnich¹², T. Shimizu¹, F. Snik¹⁵, E. Sturm¹, L. J. Tacconi¹, W. Taylor¹³, A. Valentini¹¹, C. Waring¹³, and M. Xompero¹⁰

(Affiliations can be found after the references)

Draft version October 2, 2025

ABSTRACT

The black hole in the Galactic Center, Sgr A*, is prototypical for ultra-low-fed galactic nuclei. The discovery of a hand-full of gas clumps in the realm of a few Earth masses in its immediate vicinity provides a gas reservoir sufficient to power Sgr A*. In particular, the gas cloud G2 is of interest due to its extreme orbit, on which it passed at a pericenter distance of around 100 AU and notably lost kinetic energy during the fly-by due to the interaction with the black hole accretion flow. 13 years prior to G2, a resembling gas cloud called G1, passed Sgr A* on a similar orbit. The origin of G2 remained a topic of discussion, with models including a central (stellar) source still proposed as alternatives to pure gaseous clouds. Here, we report the orbit of a third gas clump moving again along (almost) the same orbital trace. Since the probability of finding three stars on close orbits is very small, this strongly argues against stellar-based source models. Instead, we show that the gas streamer G1-2-3 plausibly originates from the stellar wind of the massive binary star IRS16SW. This claim is substantiated by the fact that the small differences between the three orbits - the orientations of the orbital ellipses in their common plane as a function of time - are consistent with the orbital motion of IRS 16SW.

Key words. black hole physics – Galaxy: nucleus – gravitation – relativistic processes

1. Introduction

1.1. Observed properties of G2

The peculiar object G2 in the Galactic Center was detected in Gillessen et al. (2012) as an object apparently residing between the S-stars (Eckart & Genzel 1996; Ghez et al. 1998; Schödel et al. 2002; Ghez et al. 2003; Eisenhauer et al. 2005; Ghez et al. 2008; Gillessen et al. 2009; Gillessen et al. 2017; Gravity Collaboration et al. 2024). G2 showed the properties of a dusty, ionized gas cloud: Line emission from hydrogen and helium, and thermal emission corresponding to 600 K. No emission from a potential stellar photosphere (with $T \gtrsim 3000$ K) was convincingly detected, as the claimed K-band detection in Eckart et al. (2013) remained episodic. G2 was spatially marginally resolved (at the ~ 60 mas resolution of the 8m VLT in K-band), but more importantly showed spectrally a velocity gradient across the source.

Multi-year adaptive optics imaging (with NACO, Lenzen et al. 1998; Rousset et al. 1998) and integral field spectroscopy (with SINFONI Eisenhauer et al. 2003; Bonnet et al. 2003) in the near-infrared showed that G2 was approaching Sgr A* on a very eccentric orbit with a pericenter passage in 2014 (Witzel et al. 2014; Gillessen et al. 2013). Position-velocity diagrams of the following years showed a spectacular tidal evolution of the gas stretching along the orbital trace (Pfuhl et al. 2015; Plewa et al. 2017).

Given the measured size of around 120 AU and the thermal luminosity and temperature, it was clear that G2 is optically thin and fully ionized by the UV photons of the surrounding young, massive stars. From the Brackett- γ luminosity, and assuming case B recombination theory, the gas mass of G2 was estimated to be $\lesssim 3$ Earth masses.

With the gas of G2 nearly radially falling in, a number of papers addressed the question, whether there would be a radiative reaction observable around pericenter passage (Gillessen et al. 2012; Narayan et al. 2012; Crumley & Kumar 2013; Bartos et al. 2013). The absence of any such events does, however, not yield any strong constraint on possible source models. Ponti et al. (2015) report a mildly increased rate of X-ray flares from Sgr A* post-pericenter passage of G2.

Pfuhl et al. (2015) noted that 12 years ahead of G2, a very similar, although a bit fainter, object was moving along a very similar trajectory, which they called G1. The dust emission of this object was also noted already in very early adaptive-optics images (Clénet et al. 2005), where it appeared spatially extended (Ghez et al. 2005), and also showed tidal evolution along the orbit (Witzel et al. 2017). Further, a tail follows behind G2 on apparently a similar orbit. One could thus think of G1, G2 and the tail being knots in a long gas streamer, of which we detect in sensitivity-limited observations only the brightest peaks, aided by the fact that the observed surface brightness of the gas scales like density squared.

The long gas streamer actually is visible in deep spectroscopic integrations (see figures 9 and 10 in Plewa et al. 2017). It points spatially and in radial velocity back to the stellar wind of the contact binary system IRS 16SW (Ott et al. 1999; Martins et al. 2006). That star is classified as Ofpe/WN9 type and a member of the clockwise (CW) disk of young stars (Levin & Beloborodov 2003; Paumard et al. 2006; Lu et al. 2009; Bartko et al. 2009; Yelda et al. 2014; von Fellenberg et al. 2022; Jia et al. 2023), and G2 and G1 orbit Sgr A* in that same plane. In hydrodynamical simulations (Cuadra et al. 2006; Calderón et al. 2020b) the star is a significant contributor to the gas found around Sgr A*, and observationally its spectrum shows signs of strong winds.

The post-pericenter motion of G2 is actually better described by adding a ram-pressure-like drag force to the Keplerian model (Pfuhl et al. 2015; McCourt & Madigan 2016; Madigan et al. 2017; Gillessen et al. 2019). G2 decelerates due the interaction with the accretion flow of Sgr A* (Yuan et al. 2003; Yuan & Narayan 2014), the density of which follows roughly a radial profile $\propto r^{-1}$. G2's motion provides thus a valuable measurement of the accretion flow density at around 10^3 Schwarzschild radii r_S , which otherwise is constrained mostly around $10r_S$ from submm observations (Agol 2000; Quataert & Gruzinov 2000; Bower et al. 2003; Marrone et al. 2006, 2007; Bower et al. 2015), or around $10^5 r_S$ from X-ray observations (Baganoff et al. 2003; Wang et al. 2013).

1.2. Source models for G2

Given the strong evidence for gaseous, tidal evolution in G2, it is clear that the observed gas cannot be gravitationally bound to a central source. With the measured size of G2 (≈ 20 mas) around the time of detection (Gillessen et al. 2012), the mass required to bind gas on that scale would exceed $10^4 M_\odot$, i.e. an intermediate mass black hole, which is excluded at such small radii (Gillessen et al. 2009; Naoz et al. 2020; Reid & Brunthaler 2020; Gravity Collaboration et al. 2023). Yet, this does not exclude the possibility of a central stellar source that could be the origin of the gas.

Observationally, there is no need to invoke a central object for G2. All its properties can be explained without. It only has an L-band counterpart, but is invisible in K-band. Also the post-pericenter presence and appearance of G2 is not a strong discriminator, as purely gaseous models do not predict complete disruption of the cloud, see for example fig. 2 in Schartmann et al. (2015). Still, models with a central source have been discussed and often favored (Phifer et al. 2013; Witzel et al. 2014). Scoville & Burkert (2013) proposed a young low-mass star, the wind of which would create G2. Meyer & Meyer-Hofmeister (2012) discussed a stellar nova as origin for G2. Also, tidal interactions of a star with Sgr A* have been proposed, either from a disk around the star (Murray-Clay & Loeb 2012; Miralda-Escudé 2012) or a true, partial tidal disruption of a giant star (Guillochon et al. 2014).

Perhaps most extreme seems the proposal, that not only G2, but maybe also other, similar gas knots (Ciurlo et al. 2020) are binary merger products (Witzel et al. 2014), driven by the Kozai-Lidov mechanism (Prodan et al. 2015; Stephan et al. 2016). This picture requires a number of assumptions, from the presence and merging of binaries close to Sgr A*, to the question of how such an object would appear, and for how long it would do so, and how likely it is to observe a number of them simultaneously, given that the total number of stars from which the mergers can come is only larger by perhaps a factor of 20.

Here, we present new observational evidence supporting the gas streamer picture: The emission that formed the outer tail at the time of discovery of G2 has now shaped up to a clump that resembles very much G2 in 2008 - constituting thus a third object, which is moving along almost the same trajectory. Naturally, this clump could be called 'G3', however this name has already been taken by Ciurlo et al. (2020) for another gaseous object. Given the properties of G1, G2 and the new G3, it is anyhow more natural to think of them together as a gas streamer, which we will call G1-2-3. For the purpose of this paper G3 refers to the third gas clump in this series, but we propose to refer to it in future work as 'third clump of G1-2-3'.

2. Observations

Our data are based on adaptive-optics-assisted integral-field spectroscopy, pre-2020 with SINFONI, and since 2022 with ERIS (Davies et al. 2023). Both instruments use the same integral-field unit (IFU). We employ the 25 mas pixel scale and observe the K-band, in which we will concentrate in the analysis on the emission of Brackett- γ (vacuum rest wavelength $2.16612\mu\text{m}$). Since these data also serve the purpose of monitoring radial velocities of the S-stars, we cover a field of view of around $\pm 0.6''$ by dithering the $0.8''$ field-of-view IFU into four quadrants located $\pm 0.2''$ offset from Sgr A* in both coordinates. G3 is located around $(\Delta\alpha, \Delta\delta) = (+0.3, -0.1)''$ from Sgr A*, comfortably in the data cubes. The top row in figure 1 illustrates the ERIS data cube from summer 2024.

The exposure time is 600 s per individual data cube. Given the faintness of the line emission from G1-2-3, we typically add the data from one observing campaign lasting a few nights into a combined cube in order to reach the fainter magnitudes. Prior to adding, we align the cubes in all three dimensions, neglecting the small change of the local standard of rest (LSR). Table A.1 in the appendix summarizes the data used for G3.

3. Analysis

3.1. The orbits of G1, G2 and G3

Using QFitsView (Ott, T. 2025), we identify the G3 emission around Brackett- γ . For obtaining an estimate of G3's orbit, we measure the position and radial velocity of the emission line. Since it is extended both spatially and spectrally, this is done manually, trying to capture the major part of the emission around its peak. The bottom row of figure 1 shows an example for the data cube from summer 2024. The spectral and spatial line positions are obtained via simple Gaussian fits. Using the pixel scale of 12.5 mas/pix, positions are referenced to Sgr A* via S2, the orbit of which is known to much better precision than what is needed for G3. For the radial velocities we apply the standard LSR correction. Due to the extended nature we assign conservative error bars of 10 mas spatially (at least) and 50 km/s spectrally. We obtain positions from six, and radial velocities from eight epochs between 2014 and 2025 in this way. For G2 we obtain compared to Gillessen et al. (2019) in the same way five more ERIS-based radial velocities and four more positions, yielding a total of 23 velocities and 18 positions.

At this point, the G3 astrometry shows no significant acceleration towards Sgr A*, but a $> 9\sigma$ significant change of radial velocity is observed, such that we have enough dynamic quantities to determine an orbit (with six degrees of freedom) in a fixed gravitational potential. The data are shown in figure 2. A preliminary orbit fit for G3 (table B.1) shows that its orbital plane,

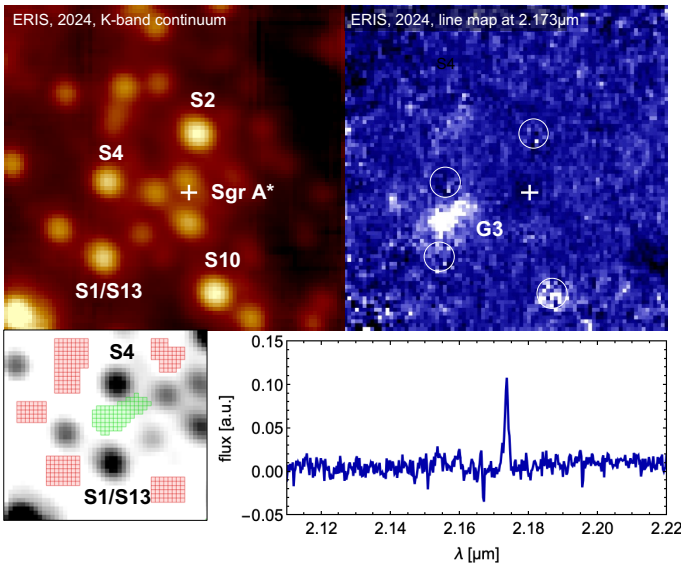


Fig. 1: G3 in the ERIS integral-field data from summer 2024. Top left: Continuum image showing the S-stars. Top right: Background-subtracted line map centered at $2.173\mu\text{m}$, corresponding to Brackett- γ + 1000 km/s. G3 stands out. Bottom left: Example of a pixel selection (on - green, off - red) for extracting the G3 spectrum overlaid on the continuum map. Bottom right: The resulting spectrum shows a strong emission line at $2.173\mu\text{m}$.

orientation, shape and size are similar to the one of G2 (and thus also close to the CW disk and G1, Pfuhl et al. 2015). Finding three objects by chance on such similar orbits is very unlikely: The probability for two orbital planes to agree to within $\pm\theta$ is $p_1 = 2\pi(1 - \cos\theta)/4\pi$; the probability that the orientations of the ellipses in the plane agree to within $\pm\theta$ is $p_2 = \theta/\pi$. Finding three orbital planes has thus a probability of $p = p_1^2 p_2$, which evaluates to $p = 2 \times 10^{-6}$ for $\theta = 15^\circ$. Similarity in orbital phase, eccentricity, and semi-major axis further reduce p . Hence, one can exclude a random alignment.

This is the motivation for our proposed model: The three clumps share (almost) identical orbits, due to their common origin from IRS 16SW. We thus fit the three orbits with strong side constraints: They need to be coplanar, and they need to share a common semi-major axis and eccentricity. The only differences allowed are thus the time of pericenter passage, and the longitude of periastron corresponding to the orientation of the orbital ellipses in their common plane. The gravitational potential is taken from GRAVITY Collaboration et al. (2022) and kept fixed ($M = 4.296 \times 10^6 M_\odot$, $R_0 = 8.275$ kpc). The drag force model is used (and fit for) as in Gillessen et al. (2019). The resulting model is shown on top of the data in figure 2. It is a very good description of the data, which is a very remarkable finding. Fitting the G2, G1, and G3 individually with each fit having six free parameters (and G2 a drag force parameter in addition) leads to χ^2 values of 115.6, 36.5, and 26.4 for 50, 14, and 14 degrees of freedom respectively. This is a total χ^2 of 178.5. The combined fit is only slightly worse with $\chi^2 = 196.6$, despite having eight free parameters less. For another representation of the combined fit see figure C.1, and section B for the orbital elements.

The apocenter distance of the orbits is around $1.9''$, occurring around the mid of the 19th century. The apocenters are not far away from where IRS 16SW was at the time (using the orbit from Gillessen et al. 2017). An exact agreement is anyhow

not expected, as the gas clumps originate from the winds of IRS 16SW (or shocks created by them), which themselves have a significant velocity of a few hundred km/s. Also the orbital planes do not agree perfectly, but differ by $\lesssim 30^\circ$, which again might just reflect the fact that the initial conditions of the gas clouds do not need to be exactly the ones of the star. If fit individually, G2 would attain a larger apocenter distance, and G3 a smaller one. This indeed might be more realistic, as individual clumps arising in the stellar wind are free to have different initial conditions. In that view, also the orbital planes can differ a bit between the three clumps and the star. Also, previous work found that the best fits of the orbits of G1 and G2 do not completely agree (Pfuhl et al. 2015; Witzel et al. 2017). But the point of the combined fit employed here is that it is remarkable, that the model in which G1 and G3 only have two free parameters each (pericenter time and longitude of pericenter) describes the data that well.

Using the combined fit, G3's pericenter passage will occur 17.6 ± 0.3 yr after the one of G2, i.e. in mid 2031. The longitudes of pericenter differ by $12.9 \pm 1.1^\circ$ between G2 and G3, with the G3 orbit being rotated clockwise against the G2 orbit. These two numbers correspond to an angular speed of $0.74 \pm 0.07^\circ/\text{yr}$. For G1 in comparison with G2, the same comparison yields an angular speed of $0.74 \pm 0.10^\circ/\text{yr}$ in the same direction (consistent with the value implied in Pfuhl et al. (2015) of $0.95 \pm 0.63^\circ/\text{yr}$). Note that the numbers happen to be very close to each other, this was not a constraint for the fit. Further, the value is remarkably close to the angular speed of IRS 16SW, which is around $1.11 \pm 0.32^\circ/\text{yr}$ at its orbits around 1950. Thus, **the differences between the G1, G2 and G3 orbits can be explained by the orbital motion of IRS 16SW**. This is an additional hint towards the star being the origin of the gas clouds. We note that other (clockwise disk) stars in the vicinity could in principle also be responsible for the production of the gas clumps. Here we limit ourselves to discussing IRS 16SW, which we consider to be the most likely candidate.

3.2. Position velocity diagram for G3

Using the same technique as in Gillessen et al. (2019) of extracting a position-velocity diagram along the curved trajectory given by the orbit, we obtain the diagram shown in figure 3. The G3 emission resembles very much G2 a few years before pericenter passage. Notably, also G3 shows trailing emission, like G2 showed a tail as noted already in the discovery paper Gillessen et al. (2012). The Brackett- γ luminosity of G3 is comparable to that of G2, although roughly 38% lower.

4. Discussion

With the ample hints of G1-2-3 being related to IRS 16SW, it is worth re-considering the formation of gas clumps from the winds of that source. This requires the production of clouds with masses of \lesssim few Earth masses at intervals of 10–20 years, yielding a time-averaged mass rate on the order of $\sim 10^{-7} M_\odot \text{ yr}^{-1}$. This constitutes a non-negligible fraction of around 1% of the Wolf-Rayet wind rate of $\sim 10^{-4.7} M_\odot \text{ yr}^{-1}$ (Martins et al. 2007). Channelling such a substantial fraction of an initially quasi-spherical outflow toward the central SMBH poses a significant dynamical challenge as the gas has to lose most of its orbital angular momentum. An anisotropic mass-loading geometry, possibly governed by the orientation of IRS 16SW binary axis relative to its orbital motion, may be required to facilitate such an efficient mass transfer. Unfortunately, the orientation of the orbit is

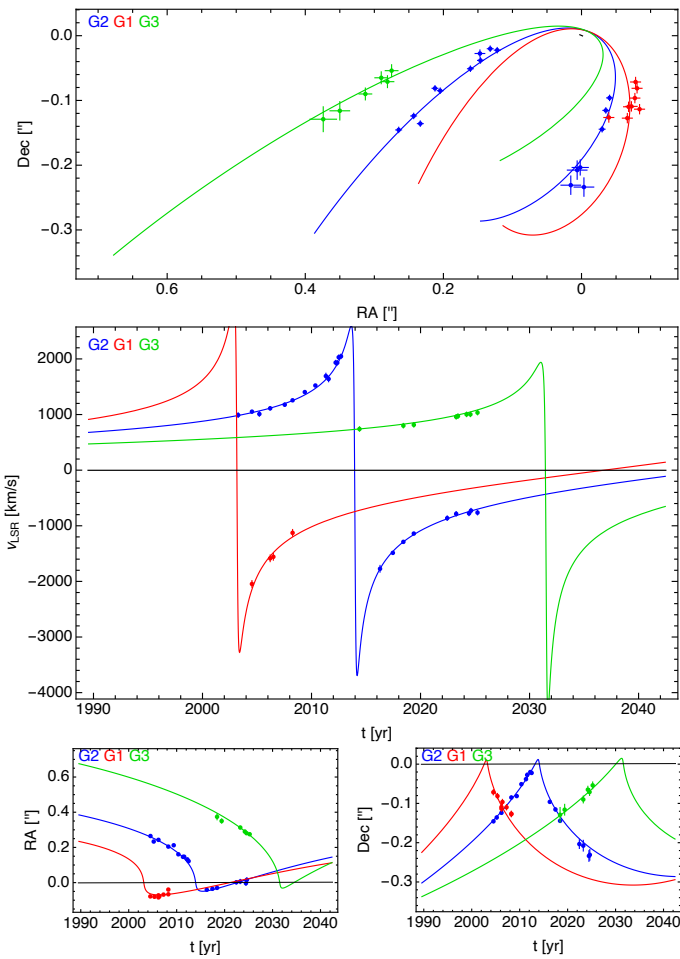


Fig. 2: The orbits and data of G1, G2 and G3, fit under the side constraint that they share the same orbital plane, semi-major axis and eccentricity. Top: On-sky appearance of the two orbits. Middle: The radial velocities. Bottom: The spatial coordinates as a function of time. The non-Keplerian shapes are a result of the drag force acting on G2 and G3 when they are close to Sgr A*.

unknown, except that the system is close to edge-on since it is observed as an eclipsing binary (Martins et al. 2006).

An alternative is to consider the interaction between stellar winds and the medium. In the central light-month around Sgr A*, we expect the formation of clumps in the shocks produced by stellar winds, where a dense slab can form. This slab, depending on its radiative properties, can be prone to cooling and hydrodynamic instabilities that result into the formation of clumps (Vishniac 1994). This process has been studied analytically and numerically for stellar wind collisions in binaries and random stellar encounters (Calderón et al. 2016, 2020a). These works found that for the Galactic Center stars, the clumps formed are smaller and lighter than those observed. Additionally, Calderón et al. (2018) investigated the hypothesis of binaries, specifically focusing on IRS 16SW, launching clumps into the medium and following their ballistic orbits. The results showed that it was not possible to reproduce the position and velocity of G2 provided it formed from the binary. Interestingly, the simulations of Calderón et al. (2020b, 2025) of the whole Wolf-Rayet population in the Galactic centre revealed a different formation mechanism that actually relied on the hydrodynamic interaction with the medium, namely, the disruption of the wind bow shock.

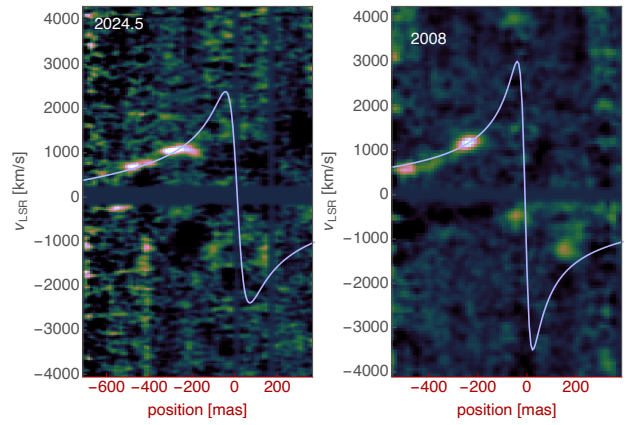


Fig. 3: Left: Position-velocity diagram extracted from the summer-2024 data cube, using a curved slit along the orbital trace of G3. The emission of G3 is concentrated around $(-300 \text{ mas}, +1000 \text{ km/s})$. Like G2, G3 seems to be followed by a tail, indicative of even more material flowing along the G1-2-3 path. Right: For comparison, the same diagram for G2 extracted from the 2008 data cube (from Gillessen et al. 2019).

For that, the medium needs to be relatively dense, and the stellar wind needs to have a low terminal velocity, typically 450 km s^{-1} .

Previous models of the Galactic centre hydrodynamics (e.g. Cuadra et al. 2008, 2015; Ressler et al. 2018; Calderón et al. 2025) used 600 km s^{-1} for the stellar wind of IRS 16SW, based on its spectral features (Martins et al. 2007; Cuadra et al. 2008). While relatively low, that velocity did not result in the formation of an unstable bow shock in the models. IRS16SW however is a close binary, so its outflow velocity can be very different from that determined by its atmospheric properties. High-resolution simulations of collisions of winds in static stellar pairs by Calderón et al. (2020a) found that clumps formed by a symmetric binary tend to be ejected at $\approx 3/5$ of the individual stellar wind velocity, so 360 km s^{-1} in this case. While the orbit of the binary was not included in the model, we expect that its internal velocity (also around 360 km s^{-1}) can be added to or subtracted from the outflowing material, resulting in a range of effective velocities for the outflow from 0 to $\approx 700 \text{ km s}^{-1}$. The low velocities could result in bow shocks as described above.

To test this idea, we ran a simulation of the Wolf-Rayet stellar winds feeding Sgr A* using the setup of the control model (without feedback from Sgr A*) of Cuadra et al. (2015). The system of 30 mass-losing stars was placed on their observed orbits (Cuadra et al. 2008; Gillessen et al. 2017) with their constrained stellar wind properties (Martins et al. 2007; Cuadra et al. 2008), and evolved for 1100 yr but starting in the past in order to recover the state of the system at the present time. Different than in our previous work, we made use of the state-of-the-art smoothed-particle hydrodynamic (SPH) code Phantom (Price et al. 2018, Russell et al. in prep.) in order to avoid the formation of spurious clumps in the generic SPH technique (e.g. Hobbs et al. 2013). While ideally IRS 16SW should be modelled as a binary, its compactness makes that impossible with our current setup. We therefore explore the effect of its expected slower wind by modelling it as a single source with wind speeds of 300 km s^{-1} , 400 km s^{-1} , and 600 km s^{-1} . The latter being equivalent to previous works in the literature (e.g. Cuadra et al. 2008, 2015; Ressler et al. 2018; Calderón et al. 2020b). The simulations with 300 km s^{-1} and 400 km s^{-1} do result in the formation of a dense bow shock around this source, which gets disrupted

into several clumps and filaments, some of which get in orbits towards Sgr A* (see Figure 4), staying roughly in the same orbital plane as the source. The clumps produced in the simulations also have masses of the same order of magnitude as the observed ones. These results differ from the conclusions of Calderón et al. (2018) because in the current models the clumps form in the bow shock in front of IRS 16SW’s orbit, and not at the binary location itself. The bow shock slows down the material and directs it preferentially in radial orbits towards Sgr A*. So it seems possible that G1-2-3 originates from IRS16SW, although its exact origin would need to be determined from more detailed work.

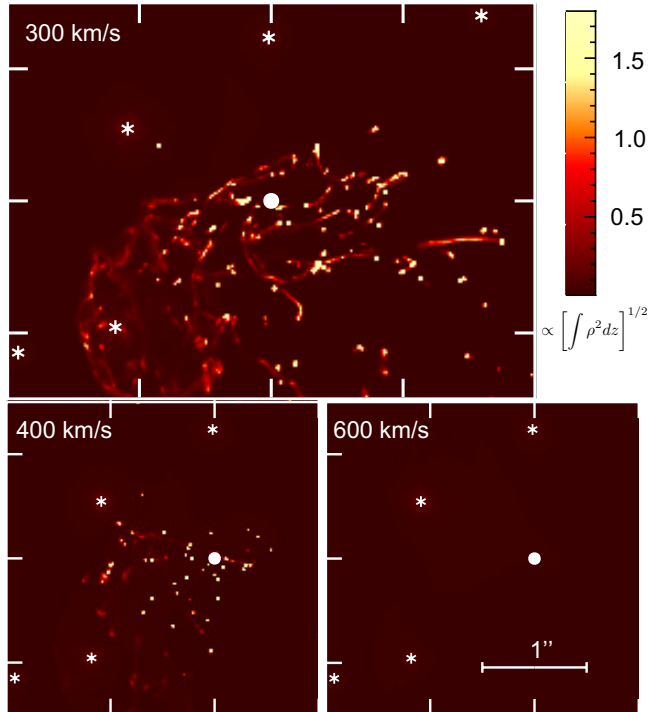


Fig. 4: Snapshots of the hydrodynamic simulations of the Wolf-Rayet stars (white asterisks) feeding Sgr A* (white disk) in the central parsec. The maps show density square integrated along the the line of sight in square root scale, i.e. $[\int \rho^2 dz]^{1/2}$, representing the expected Brackett- γ flux. Each panel represents a simulation run varying the wind speed of IRS 16SW: 300 km s⁻¹ (top), 400 km s⁻¹ (bottom left), and 600 km s⁻¹ (bottom right). The production of clumps on the scale shown here is dominated by IRS16 SW. Snapshots created with Splash (Price 2007).

Finally, it is worth noting that accreting a single G2-like clump (with a mass ≈ 1 Earth mass) per decade suffices to explain the inferred accretion rate onto Sgr A* of $\approx 10^{-7.6} M_\odot$ yr⁻¹ estimated at the apocenter distance of G2 of $\approx 1000 R_\odot$ (Yuan & Narayan 2014; Gillessen et al. 2019), i.e. the G1-2-3 streamer being decelerated by the drag force could be the main source of gas for Sgr A* currently, if the gas ≈ 50 yr after first pericenter settles into the accretion flow. This notion is in agreement with the generally accepted idea that Sgr A* is mostly fed directly by the hot plasma created by the stellar winds (Quataert et al. 1999; Cuadra et al. 2006), but is even more specific. The process creating clumps happens preferentially when IRS 16SW approaches its pericentre, as it is currently happening, where the medium is denser, and it therefore not necessarily representative of a steady state. This could relate to the variable Sgr A* emission on the time scales of decades to centuries as witnessed from X-ray reflection echoes (Clavel et al. 2013; Chuard et al. 2018).

5. Conclusions

New near-infrared IFU data from the Galactic Center reveal a third object, looking alike and moving along (roughly) the same orbit as previously G1 and G2 did, although 18 years later. Given that by probabilistic arguments it is de facto excluded to find three stellar sources in such a configuration, the new data render a stellar model at least for these three sources very unlikely. A much better picture is that of a gas streamer G1-2-3, which appears to originate from a young, massive, binary star in the clockwise disk of stars - IRS16SW. The dominant differences between the orbits of the three gas clouds are the pericenter times and orientations of the (initial) orbital ellipses in their planes. These change systematically and synchronously with the motion of IRS16SW. We conclude that G1-2-3 most likely originates from the winds of that star. Updated hydrodynamic simulations show that taking into account lower wind velocities, as they occur around binaries, IRS16SW may well be able to produce clumps and filaments of gas that can reach Sgr A*.

Acknowledgements. We are very grateful to our funding agency MPG, to ESO and the Paranal staff, and to the many scientific and technical staff members in our institutions, who helped to design, build, test, commission and operate ERIS. Based on observations collected at the European Southern Observatory under the ESO programmes listed in appendix A. The research of DC has been funded by the Alexander von Humboldt Foundation. JC acknowledges financial support from ANID – FONDECYT Regular 1211429 and 1251444, and Millennium Science Initiative Program NCN2023_002. The research of TP was supported by an advanced ERC grant ‘multijets’.

References

Agol, E. 2000, ApJ, 538, L121
 Baganoff, F. K., Maeda, Y., Morris, M., et al. 2003, ApJ, 591, 891
 Bartko, H., Martins, F., Fritz, T. K., et al. 2009, ApJ, 697, 1741
 Bartos, I., Haiman, Z., Kocsis, B., & Márka, S. 2013, Phys. Rev. Lett., 110, 221102
 Bonnet, H., Ströbele, S., Biancat-Marchet, F., et al. 2003, Proc. SPIE Vol., 4839, 329
 Bower, G. C., Markoff, S., Dexter, J., et al. 2015, ApJ, 802, 69
 Bower, G. C., Wright, M. C. H., Falcke, H., & Backer, D. C. 2003, ApJ, 588, 331
 Calderón, D., Ballone, A., Cuadra, J., et al. 2016, MNRAS, 455, 4388
 Calderón, D., Cuadra, J., Russell, C. M. P., et al. 2025, A&A, 693, A180
 Calderón, D., Cuadra, J., Schartmann, M., et al. 2018, MNRAS, 478, 3494
 Calderón, D., Cuadra, J., Schartmann, M., et al. 2020a, MNRAS, 493, 447
 Calderón, D., Cuadra, J., Schartmann, M., Burkert, A., & Russell, C. M. P. 2020b, ApJ, 888, L2
 Chuard, D., Terrier, R., Goldwurm, A., et al. 2018, A&A, 610, A34
 Ciurlo, A., Campbell, R. D., Morris, M. R., et al. 2020, Nature, 577, 337
 Clavel, M., Terrier, R., Goldwurm, A., et al. 2013, A&A, 558, A32
 Clénet, Y., Rouan, D., Gratadour, D., et al. 2005, A&A, 439, L9
 Crumley, P. & Kumar, P. 2013, MNRAS, 436, 1955
 Cuadra, J., Nayakshin, S., & Martins, F. 2008, MNRAS, 383, 458
 Cuadra, J., Nayakshin, S., Springel, V., & Di Matteo, T. 2006, MNRAS, 366, 358
 Cuadra, J., Nayakshin, S., & Wang, Q. D. 2015, MNRAS, 450, 277
 Davies, R., Absil, O., Agapito, G., et al. 2023, A&A, 674, A207
 Eckart, A. & Genzel, R. 1996, Nature, 383, 415
 Eckart, A., Mužić, K., Yazici, S., et al. 2013, A&A, 551, A18
 Eisenhauer, F., Abuter, R., Bickert, K., et al. 2003, in Proc. SPIE, Vol. 4841, Instrument Design and Performance for Optical/Infrared Ground-based Telescopes, ed. M. Iye & A. F. M. Moorwood, 1548–1561
 Eisenhauer, F., Genzel, R., Alexander, T., et al. 2005, ApJ, 628, 246
 Ghez, A., Duchêne, G., Matthews, K., et al. 2003, ApJ Letters, 586, 127
 Ghez, A., Salim, S., Weinberg, N. N., et al. 2008, ApJ, 689, 1044
 Ghez, A. M., Hornstein, S. D., Lu, J. R., et al. 2005, ApJ, 635, 1087
 Ghez, A. M., Klein, B. L., Morris, M., & Becklin, E. E. 1998, ApJ, 509, 678
 Gillessen, S., Eisenhauer, F., Trippe, S., et al. 2009, ApJ, 692, 1075
 Gillessen, S., Genzel, R., Fritz, T. K., et al. 2013, ApJ, 774, 44
 Gillessen, S., Genzel, R., Fritz, T. K., et al. 2012, Nature, 481, 51
 Gillessen, S., Plewa, P. M., Eisenhauer, F., et al. 2017, ApJ, 837, 30
 Gillessen, S., Plewa, P. M., Widmann, F., et al. 2019, ApJ, 871, 126
 Gravity Collaboration, Abd El Dayem, K., Abuter, R., et al. 2024, A&A, 692, A242

GRAVITY Collaboration, Abuter, R., Aimar, N., et al. 2022, A&A, 657, L12
 Gravity Collaboration, Straub, O., Bauböck, M., et al. 2023, A&A, 672, A63
 Guillochon, J., Loeb, A., MacLeod, M., & Ramirez-Ruiz, E. 2014, ApJ, 786, L12
 Hobbs, A., Read, J., Power, C., & Cole, D. 2013, MNRAS, 434, 1849
 Jia, S., Xu, N., Lu, J. R., et al. 2023, ApJ, 949, 18
 Lenzen, R., Hofmann, R., Bizenberger, P., & Tusche, A. 1998, Proc. SPIE Vol., 3354, 606
 Levin, Y. & Beloborodov, A. M. 2003, ApJ, 590, L33
 Lu, J. R., Ghez, A. M., Hornstein, S. D., et al. 2009, ApJ, 690, 1463
 Madigan, A.-M., McCourt, M., & O'Leary, R. M. 2017, MNRAS, 465, 2310
 Marrone, D. P., Moran, J. M., Zhao, J.-H., & Rao, R. 2006, ApJ, 640, 308
 Marrone, D. P., Moran, J. M., Zhao, J.-H., & Rao, R. 2007, ApJ, 654, L57
 Martins, F., Genzel, R., Hillier, D. J., et al. 2007, A&A, 468, 233
 Martins, F., Trippe, S., Paumard, T., et al. 2006, ApJ, 649, L103
 McCourt, M. & Madigan, A.-M. 2016, MNRAS, 455, 2187
 Meyer, F. & Meyer-Hofmeister, E. 2012, A&A, 546, L2
 Miralda-Escudé, J. 2012, ApJ, 756, 86
 Murray-Clay, R. A. & Loeb, A. 2012, Nature Communications, 3, 1049
 Naoz, S., Will, C. M., Ramirez-Ruiz, E., et al. 2020, ApJ, 888, L8
 Narayan, R., Özel, F., & Sironi, L. 2012, ApJ, 757, L20
 Ott, T., Eckart, A., & Genzel, R. 1999, ApJ, 523, 248
 Ott, T. 2025, QfitsView, <https://www.mpe.mpg.de/~ott/QFitsView/>
 Paumard, T., Genzel, R., Martins, F., et al. 2006, ApJ, 643, 1011
 Pfuhl, O., Gillessen, S., Eisenhauer, F., et al. 2015, ApJ, 798, 111
 Phifer, K., Do, T., Meyer, L., et al. 2013, ApJ, 773, L13
 Plewa, P. M., Gillessen, S., Pfuhl, O., et al. 2017, ApJ, 840, 50
 Ponti, G., De Marco, B., Morris, M. R., et al. 2015, MNRAS, 454, 1525
 Price, D. J. 2007, PASA, 24, 159
 Price, D. J., Wurster, J., Tricco, T. S., et al. 2018, PASA, 35, e031
 Prodan, S., Antonini, F., & Perets, H. B. 2015, ApJ, 799, 118
 Quataert, E. & Gruzinov, A. 2000, ApJ, 539, 809
 Quataert, E., Narayan, R., & Reid, M. J. 1999, ApJ, 517, L101
 Reid, M. J. & Brunthaler, A. 2020, ApJ, 892, 39
 Ressler, S. M., Quataert, E., & Stone, J. M. 2018, MNRAS, 478, 3544
 Rousset, G., Lacombe, F., Puget, P., et al. 1998, Proc. SPIE Vol., 3353, 508
 Schartmann, M., Ballone, A., Burkert, A., et al. 2015, ApJ, 811, 155
 Schödel, R., Ott, T., Genzel, R., et al. 2002, Nature, 419, 694
 Scoville, N. & Burkert, A. 2013, The Astrophysical Journal, 768, 108
 Stephan, A. P., Naoz, S., Ghez, A. M., et al. 2016, MNRAS, 460, 3494
 Vishniac, E. T. 1994, ApJ, 428, 186
 von Fellenberg, S. D., Gillessen, S., Stadler, J., et al. 2022, ApJ, 932, L6
 Wang, Q. D., Nowak, M. A., Markoff, S. B., et al. 2013, Science, 341, 981
 Witzel, G., Ghez, A. M., Morris, M. R., et al. 2014, ApJ, 796, L8
 Witzel, G., Sitarski, B. N., Ghez, A. M., et al. 2017, ApJ, 847, 80
 Yelda, S., Ghez, A. M., Lu, J. R., et al. 2014, ApJ, 783, 131
 Yuan, F. & Narayan, R. 2014, ARA&A, 52, 529
 Yuan, F., Quataert, E., & Narayan, R. 2003, ApJ, 598, 301

¹ Max Planck Institute for extraterrestrial Physics, Giessenbachstraße 1, 85748 Garching, Germany

² Departments of Physics and Astronomy, Le Conte Hall, University of California, Berkeley, CA 94720, USA

³ Technical University of Munich, 85747 Garching, Germany

⁴ Universidad Adolfo Ibañez, Av. Padre Hurtado 750, Viña del Mar, Chile

⁵ Max Planck Institute for Astrophysics, Karl-Schwarzschild-Straße 1, 85748 Garching, Germany

⁶ University Observatory Munich, Scheinerstraße 1, 81679 Munich, Germany

⁷ Racah Institute for Physics, The Hebrew University, Jerusalem, 91904, Israel

⁸ Department of Physics and Astronomy, Bartol Research Institute, University of Delaware, Newark, DE 19716, USA

⁹ Millennium Nucleus on Transversal Research and Technology to Explore Supermassive Black Holes (TITANS), Chile

¹⁰ INAF – Osservatorio Astrofisico di Arcetri, Largo E. Fermi 5., 50125, Firenze, Italy

¹¹ INAF – Osservatorio Astronomico d'Abruzzo, Via Mentore Maggini, 64100, Teramo, Italy

¹² INAF – Osservatorio Astronomico di Padova, Vicoletto dell'Osservatorio 5, 35122, Padova, Italy

¹³ STFC UK ATC, Royal Observatory Edinburgh, Blackford Hill. Edinburgh, EH9 3HJ, UK

¹⁴ ETH Zurich, Institute of Particle Physics and Astrophysics, Wolfgang-Pauli-Strasse 27, 8093 Zurich, Switzerland

¹⁵ Leiden Observatory, University of Leiden, P.O. Box 9513, 2300 RA Leiden, The Netherlands

¹⁶ I. Physikalisches Institut, Universität zu Köln, Zülpicher Str. 77, 50937, Köln, Germany

Appendix A: Data

Table A.1: Integral-field spectroscopy observations used for G3

Year	ESO prog. ID	Instrument + Setup	total exposure
2014	092.B-0398(ABD)	SINFONI, H+K-band	1590 min
	093.B-0218(ABD)	SINFONI, H+K-band	
	093.B-0217(F)	SINFONI, H+K-band	
2018	299.B-5056(B)	SINFONI, H+K-band	1770 min
	598.B-0043(BDEFGHI)	SINFONI, H+K-band	
	0101.B-0195(BCDEFG)	SINFONI, H+K-band	
2019	0103.B-0026(BDF)	SINFONI, H+K-band	810 min
	5102.B-0086(Q)	SINFONI, H+K-band	
	594.B-0498(Q)	SINFONI, H+K-band	
2023	111.24H0.00(23)	ERIS, K-band	770 min
2024	112.25FZ.001	ERIS, K-band	360 min
2025	113.26B5.001	ERIS, K-band	
	114.2756.001	ERIS, K-band	340 min

Appendix B: Orbital elements

We use the classical orbital elements for the non-Keplerian orbits in the sense of osculating elements. They are semi-major axis a , eccentricity e , inclination i , position angle ascending of the ascending node Ω , longitude of the pericenter ω and epoch of pericenter passage t_p . The mass M of Sgr A* and its distance R_0 are kept fixed. For the individual fits, we include the drag force parameter (Gillessen et al. 2019) as a free parameter for G2, and use the resulting best-fit value as fixed quantity for the much less constrained G1 and G3 fits. The uncertainties are the formal fit uncertainties, rescaled such the reduced χ^2 of each fit is 1. The orbit of G1 with our data is only poorly constrained, especially in a and e , where the formal uncertainties don't properly represent the posterior space. Comparing with Witzel et al. (2017) and/or including their data for increased phase coverage in our fits, leads to a semi-major axis value comparable with that of G2, and an eccentricity of around $e = 0.98$.

Table B.1: Orbit parameters for the individual orbit fits

Parameter	G2	G1	G3
a ["]	1.50 ± 0.41	0.23 ± 0.06	0.92 ± 0.69
e	0.989 ± 0.003	0.76 ± 0.08	0.978 ± 0.0029
i [°]	122.0 ± 0.8	112.8 ± 3.9	126.1 ± 8.7
Ω [°]	70.0 ± 3.3	59.0 ± 8.1	49.7 ± 49.3
ω [°]	94.6 ± 2.3	97.41 ± 8.8	91.5 ± 33.1
t_p	2014.18 ± 0.12	2002.8 ± 0.7	2033.6 ± 2.5
χ^2_{red}	2.31	2.76	1.89

Table B.2: Orbit parameters for the common orbit fit

Parameter	Value	formal fit error
a ["]	0.9540	0.0810
e ["]	0.98111	0.0019
i [°]	120.14	0.35
Ω [°]	77.50	0.64
ω G2 [°]	99.52	0.56
t_p G2 [yr]	2013.945	0.042
ω G1 [°]	91.57	0.91
t_p G1 [yr]	2003.123	0.075
ω G3 [°]	112.44	0.88
t_p G3 [yr]	2031.513	0.206

Appendix C: Additional illustration

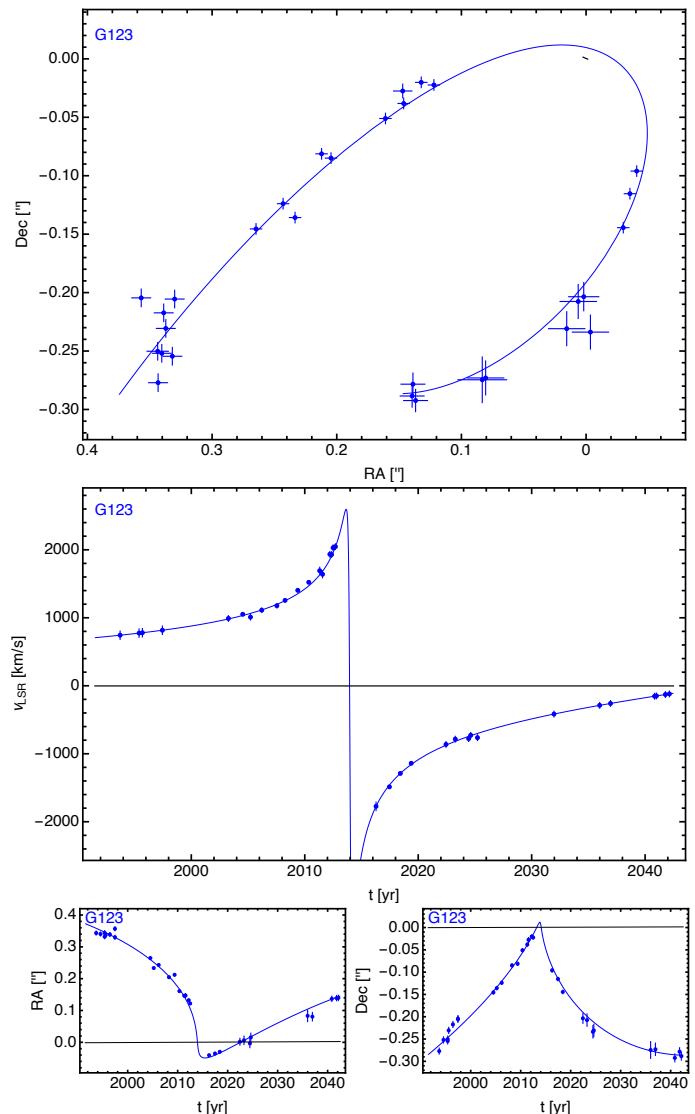


Fig. C.1: Alternative representation of the combined orbit fit for G1, G2 and G3. The data from G1 and G3 have been corrected for the differences in the respective orbits to the G2 orbit, and plotted on top of the G2 orbit and data.